NANO · MICRO small
www.small-journal.com

Nanoscale FasL Organization on DNA Origami to Decipher Apoptosis Signal Activation in Cells

Ricarda M. L. Berger, Johann M. Weck, Simon M. Kempe, Oliver Hill, Tim Liedl, Joachim O. Rädler, Cornelia Monzel, and Amelie Heuer-Jungemann**

Cell signaling is initiated by characteristic protein patterns in the plasma membrane, but tools to decipher their molecular organization and activation are hitherto lacking. Among the well-known signaling pattern is the death inducing signaling complex with a predicted hexagonal receptor architecture. To probe this architecture, DNA origami-based nanoagents with nanometer precise arrangements of the death receptor ligand FasL are introduced and presented to cells. Mimicking different receptor geometries, these nanoagents act as signaling platforms inducing fastest time-to-death kinetics for hexagonal FasL arrangements with 10 nm inter-molecular spacing. Compared to naturally occurring soluble FasL, this trigger is faster and 100× more efficient. Nanoagents with different spacing, lower FasL number or higher coupling flexibility impede signaling. The results present DNA origami as versatile signaling scaffolds exhibiting unprecedented control over molecular number and geometry. They define molecular benchmarks in apoptosis signal initiation and constitute a new strategy to drive particular cell responses.

1. Introduction

The astounding versatility and specificity by which biological signals are generated by cells are in part attributed to the cell's ability to form characteristic molecular complexes in the plasma membrane. These complexes transduce a signal inside the cell, whenever an adequate stimulus is captured from the environment.[1] Tools enabling acute control of such complex formation or its inhibition with effects on the signaling pathway are of primary interest in fundamental cell biology or nanomedicine.[2] While functionalized nano-probes such as nanoparticles,[3] quantum dots,[4] or nanodiscs[5] already demonstrated to elucidate cell signaling behavior, the number and spatial localization of ligands on these probes are difficult to control. DNA origami, on the other hand, is a powerful tool to build versatile DNA-based platforms[6] which satisfy multiple structural and biofunctional constraints including the possibility of complex molecular conjugation with biomolecules such as peptides or proteins with nanometric precision.[7] Such defined molecular organization can provide unique insights into ligand-receptor interactions in signaling complexes and the resulting signal transduction as well as serve to enhance or block particular signals.[8]

Among the signaling complexes which present themselves as supramolecular assemblies, receptors and ligands of the tumor necrosis factor (TNF) super family are extensively studied and models of their multimerization and cluster formation have been proposed.[9] Within this family, the trimeric Fas ligand (FasL, CD178) plays a pivotal role in cell decision making toward proliferation or apoptosis.[10] FasL is mainly expressed by lymphoid and myeloid cells and eliminates cancer cells by FasL-mediated apoptosis.[11] However, recent studies demonstrated that tumor cells may also resist FasL-induced apoptosis, presumably due to Fas-mediated activation of other receptors[12] or differences in the soluble and bound presentation of FasL.[13] For these reasons, predominant interest exists in unraveling and modulating the key parameters leading to Fas receptor (FasR, CD95) complex formation and unrestricted signaling. The present models of Fas signal initiation suggest that FasR either pre-arrange in trimers assembling into hexameric patterns on the membrane (Figure S1, Supporting Information) or remain as monomers and dimers.[9,14] Upon binding of trimeric FasL, up to three FasR may bind from different sites to the ligand. Depending on the ligand-receptor availability, they may further arrange in hexameric supramolecular structures with ≈10 nm intermolecular spacing and recruit intracellular adaptor proteins to form the death-inducing

Dr. R. M. L. Berger, S. M. Kempe, Prof. T. Liedl, Prof. J. O. Rädler
Faculty of Physics and Center for NanoScience (CeNS)
Ludwig-Maximilians-University
Geschwister-Scholl-Platz 1, 80539 Munich, Germany
J. M. Weck, Dr. A. Heuer-Jungemann
Max Planck Institute of Biochemistry and Center for Nanoscience (CeNS)
Ludwig-Maximilians-University
Am Klopferspitz 18, 82152 Martinsried, Germany
E-mail: heuer-jungemann@biochem.mpg.de
Dr. O. Hill
Apogenix AG
University of Heidelberg
Im Neuenheimer Feld 584, 69120 Heidelberg, Germany
Prof. C. Monzel
Experimental Medical Physics
Heinrich-Heine University
Universitätsstrasse 1, 40225 Düsseldorf, Germany
E-mail: cornelia.monzel@hhu.de
The ORCID identification number(s) for the author(s) of this article can be found under https://doi.org/10.1002/smll.202101678.

DOI: 10.1002/smll.202101678

signaling complex (DISC). Eventually, proximity dimerization and autocatalysis of caspases at the DISC lead to apoptosis.[9,10c,15]

So far, the role of molecular geometry of FasL for signaling complex formation was not yet demonstrated experimentally, mostly due to a lack of tools enabling acute control over molecular positioning at the nanoscale. To address this question, we designed DNA-based nanoagents consisting of a one-layer DNA origami sheet functionalized with different nanometric arrangements of FasL to act as nanometric graded signal initiators (Figure S2, Supporting Information). We then quantified the apoptotic kinetics of HeLa cells stably expressing FasR-mEGFP when exposed to these nanoagents.

First, we demonstrate fast signaling responses and a high efficiency of FasL DNA origami, which outscore apoptosis initiation mediated by FasL coupled to membranes or by the naturally occurring FasL in solution. We then investigate the role of FasL geometry on DNA origami and thereby test current signal initiation models predicting a hexagonal arrangement of FasR. Intriguingly, we identify nanoagents with hexagons of 10 nm FasL–FasL intermolecular distance as the most efficient signal initiators, whereas different hexagonal spacing and lower FasL number per DNA origami impede signal transduction or slow the kinetics. Finally, by applying different FasL coupling strategies, providing different ligand flexibility, we show that scaffold rigidity is an essential prerequisite for robust signal initiation.

Overall, the acute control over molecular number and geometry using FasL–DNA origami enables to identify molecular benchmarks in apoptosis signal initiation: rigid hexagonal FasL with 10 nm intermolecular spacing and least FasL coupling flexibility turn out to be 100× more efficient compared to soluble FasL, when FasL is presented to the cell at identical concentrations. This corroborates a popular molecular model of Fas signal initiation and demonstrates how nanoscale arrangements of FasL on DNA origami fine-tune the cell apoptosis response. Hence, together with previous works[8] our study establishes molecular scaffolds based on DNA origami as a generic approach to uncover and to drive particular cell responses.

2. Results and Discussion

The nanoagent used in this study is based on a rectangular DNA origami sheet consisting of 24 parallel interconnected helix bundles (dimensions: 100 × 70 nm), formed from a 7249 nt long circular scaffold and 200 staple strands (see Figure S2, Supporting Information).[16] In order to achieve precise nanometric arrangement of FasL, DNA staple strands containing a terminal Biotin were designed to protrude from the DNA origami at designated positions resulting in various defined binding sites for Streptavidin and subsequently FasL (**Figure 1**A). The addition of Streptavidin allowed for the conjugation of FasL, pre-trimerized via a T4-FOLDON (Figure S3, Supporting Information) and containing a C-terminal Biotin, to the DNA origami sheet. Atomic force microscopy (AFM) images show the DNA origami sheets adsorbed onto mica, displaying the designed hexagonal conformation and 10 nm inter-ligand distance of Streptavidins on each DNA origami (Figure 1B). Through analysis of transmission electron microscopy (TEM) and AFM images, we determined an average occupancy of 5 ± 0.3 Streptavidins per DNA origami where 40% ± 8% of all analyzed DNA origamis were fully decorated with six Streptavidins (Figure 1B; Figures S4 and S5, Supporting Information). Subsequently, for DNA origamis decorated with Streptavidin and FasL, successful functionalization was confirmed by AFM imaging (Figure 1C) as well as by fluorescently labeled anti-FasL antibody staining (Figures S4 and S5, Supporting Information).

Analysis of the AFM data of the nanoagent designed with a 10 nm inter-ligand spacing revealed a 76% ± 9% binding efficiency of FasL to Streptavidin anchors with a positioning accuracy of ≈5 nm estimated from the protein structures. While the positioning of Biotins on the DNA origami is nanometer precise, spatial positioning of the FasL is limited by the size

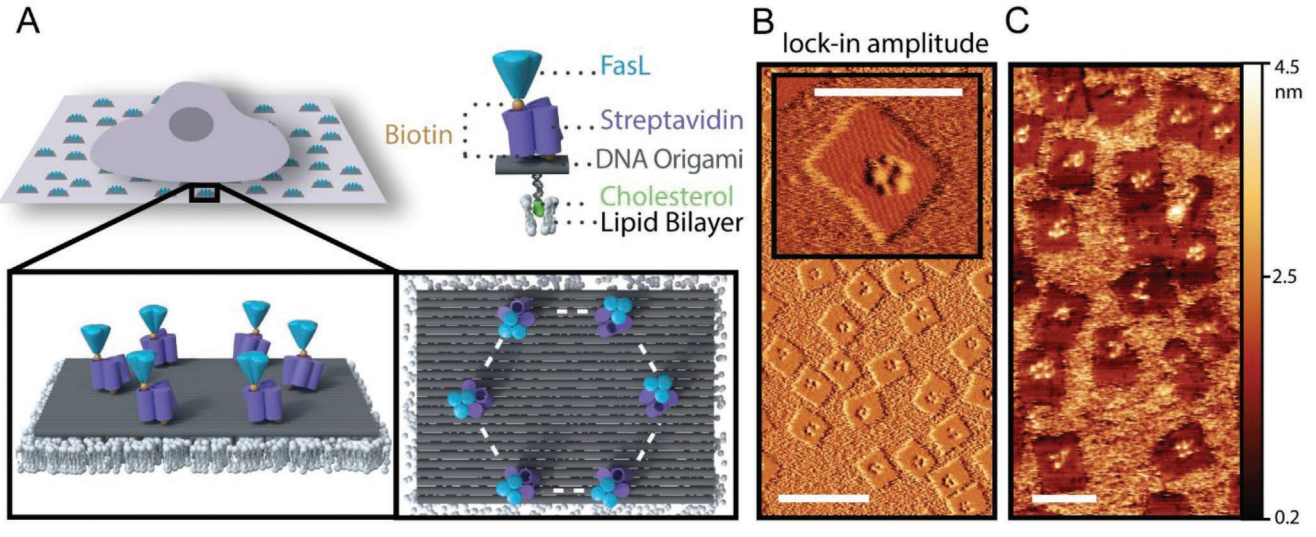

Figure 1. A) Schematic illustration of a cell seeded on DNA origami grafted to a SLM. The magnifications show the Streptavidin–Biotin mediated linkage of trimeric FasL to DNA origami. Top view illustrates the hexagonal arrangement indicated by white dashed lines. B) AFM lock-in amplitude image of Streptavidin functionalized DNA origami sheets (200 nm scale bar). The insert exemplifies the hexagonal arrangement of Streptavidin (100 nm scale bar). C) AFM height profile image of DNA origami functionalized with Streptavidin and FasL (100 nm scale bar). All images are of the nanoagent designed with a 10 nm inter-ligand spacing and unpurified to aid with imaging. Images were obtained in liquid mode on Mica.

(≈5 nm) and multivalency of wild type (wt) Streptavidin.[17] Multivalency also imposes uncertainty on the actual number of bound ligands, although due to the size of FasL and resulting steric hindrance, the attachment of more than one FasL to the same Streptavidin is highly unlikely. Nevertheless, to address this issue, we also performed experiments with monovalent (mv) Streptavidin and found similar qualitative behavior as for the multivalent Streptavidin assemblies as will be discussed later on.

Having successfully established spatially designed, multivalent nanoagents, we investigated the cell apoptosis response when exposed to FasL–DNA origamis or other FasL presentations either on a supported lipid membrane (SLM) or in solution. In order to anchor FasL–DNA origamis to the SLM, a set of 8 staple strands at the bottom side of the DNA origami were modified with Cholesterol moieties, capable of inserting into the SLM as previously reported.[18] FasL–DNA origamis adsorbed on the SLM remained oriented and laterally mobile, hence perfectly addressable to cells. For the apoptosis assay, HeLa cells overexpressing FasR were exposed to the nanoagent-functionalized SLMs and analyzed via time-lapse imaging. First, assays were carried out using FasL–DNA origamis with a hexagonal pattern and FasL–FasL distances of 10 nm, which is predicted to be the optimal distance for apoptosis induction.[9,19] Cells attaching to FasL–DNA origamis were observed to spread within the first three hours and subsequently exhibited pronounced blebbing and rounding-up, indicative of apoptosis (**Figure 2**A upper row, Movies M1 and M2 and Figure S6, Supporting Information for comparison using a Caspase 3 marker). In contrast, Huh7 cells with very low endogenous expression levels of FasR were not affected by the presence of the FasL–nanoagent (Figure S7, Supporting Information), indicating that the FasL–FasR interactions are indeed responsible for the observed apoptotic behavior. HeLa cells deposited on blank DNA origamis grafted to SLMs showed long-term normal spreading and cell division, indicating no negative effect of the bare DNA origamis on cells (Figure 2A lower row). Origami-free controls of cells, where FasL was bound to SLMs directly (via Cholesterol-DNA-Streptavidin linkers) and distributed homogeneously, as well as cells on bare SLMs in the presence of soluble FasL showed apoptosis over distinctly slower time scales and for a lower number of cells than FasL–DNA origamis with hexagonal FasL clusters. Figure 2B,C show the corresponding cell-death kinetic curves and boxplots (see Experimental Section for a description of the analysis performed). Here, the time course of the normalized cumulative sum of apoptotic events are compared for FasL–DNA origami, origami-free FasL bound to SLMs, or FasL in solution.

While for concentrations of 0.1 and 1 nM of FasL–DNA origami no significant change in the time-to-death kinetics is observed, apoptosis times for origami-free soluble and membrane-bound FasL are concentration dependent. Most importantly, a higher percentage of cells die within a short time span when subjected to FasL–DNA origamis compared to cells exposed to membrane-bound FasL or FasL in solution, which indicates that signal induction is dominated by the structural pre-arrangement of FasL. To quantitatively compare the potency of apoptosis induction of the various FasL presentations, the

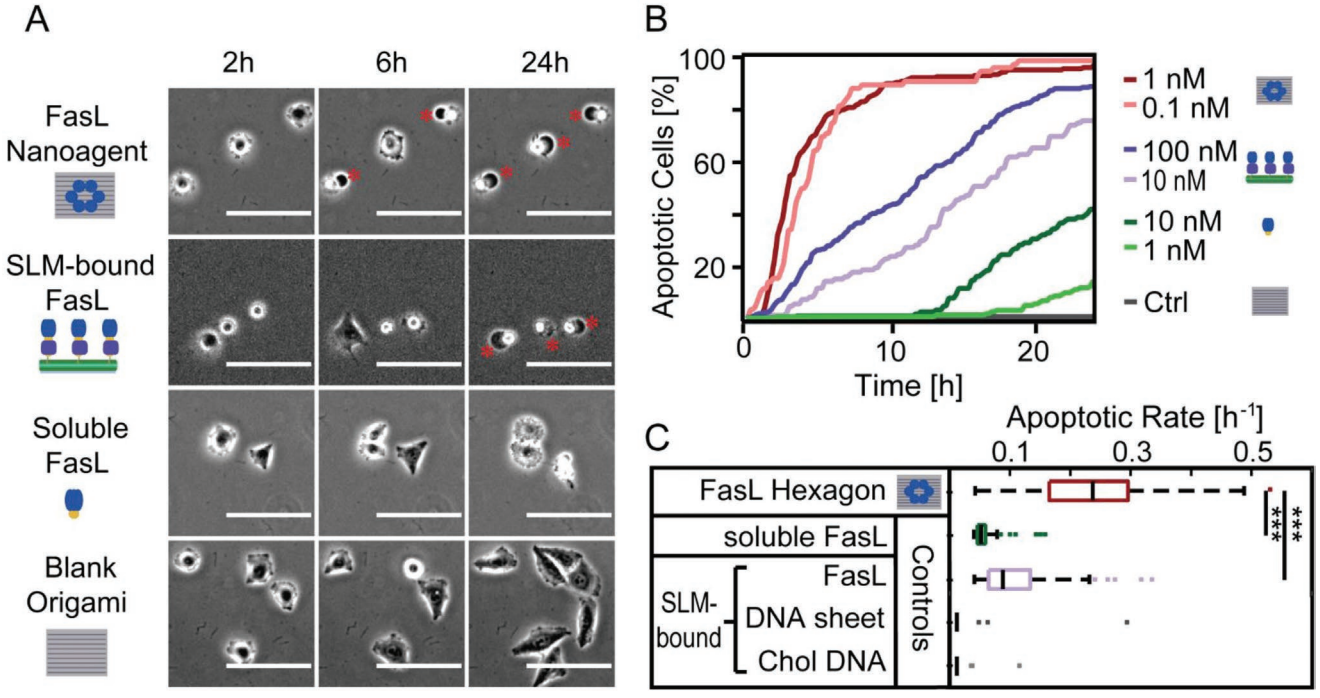

Figure 2. A) Comparison of representative bright field images showing morphological changes of cells seeded on FasL-nanoagent (10 nm hexagon), membrane-bound FasL, soluble FasL, or blank DNA origami on a SLM after 2, 6, and 24 h. Red asterisks indicate the position of the apoptotic bubble. Scale bars are 50 µm. B) Cell death kinetics from single experiments with at least 500 analyzed cells. FasL induced apoptosis is most efficient for the nanoagent (red) compared to FasL functionalized lipid membrane (lilac) and FasL in solution (green). C) Efficiency of apoptosis initiation of nanoagent compared to origami-free FasL. Median of apoptosis rate for 1 nM nanoagent is significantly higher than soluble FasL (1 nM) or membrane-bound FasL (10 nM). DNA origami sheet or Cholesterol coupled DNA do not affect cells. $n > 500$ cells/condition. Ranksum test: $^{***}p < 0.001$, $^{**}p < 0.01$, $^{*}p < 0.05$.

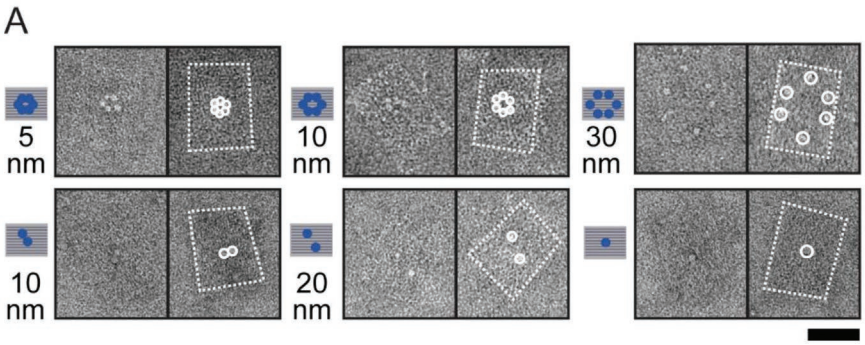

B

Design	Occupancy	Predominant Occup. Level
	66 %	4
	82 %	6
	94 %	6
	71 %	2
	74 %	2
	90 %	1

Figure 3. A) TEM images of protein coupled to DNA origami with different ligand geometries (N.B.: two different images per structure with one annotated to guide the eye). B) Corresponding ligand site occupancy for each structure and analysis of predominant occupancy level. Site occupancies were determined by analyzing >70 structures per geometry. Both Streptavidin and Streptavidin + FasL coupling to DNA origami was tested and no significant difference in occupancy levels could be observed. Scale bar is 50 nm.

time-to-death (τ_i) of all individual time courses was evaluated. We define the inverse of the individual time-to-death (τ_i) value as apoptosis rate $\left(k_i = \frac{1}{\tau_i}\right)$. Figure 2C shows box plots of the apoptosis rates derived from a minimum of 500 cells per condition and with at least two independent experiments per condition. The median of the apoptosis rates is a measure of the efficiency of apoptosis induction and turns out to be higher for FasL–DNA origamis compared to origami-free FasL, that is, membrane-bound FasL or FasL in solution. Here, this high efficiency was obtained despite the fact that membrane-bound FasL and FasL in solution are present at 10× higher concentrations compared to FasL–DNA origamis. These results are in agreement with findings by Holler et al., who fused two trimeric FasLs to form FasL-dimers based on immunoglobulins that showed elevated potency to induce apoptotic signaling.[20] In addition, Zhang et al. used a Fas peptide to target FasR and to trigger apoptosis signaling.[21] In their case, Fas peptide was coupled to a DNA tetrahedron to increase its local concentration, which resulted in an eightfold higher potency relative to the soluble peptide (5 μM versus 40 μM Fas peptide concentration). Note, that in comparison to their study, our FasL-nanoagents displayed a significantly higher potency while the concentration of nanoagent was four to five orders of magnitude lower (0.1 nM).[21] Overall, these results demonstrate that oriented and spatially pre-clustered FasL exhibit maximal efficiency to induce cell death signaling.

Having established the excellent potency of FasL–DNA origamis in comparison to membrane-bound or solube FasL, we next performed a series of proof-of-concept experiments to uncover how the nanometric arrangement of FasL affects the signaling initiation for apoptosis. To this end, three sizes of hexagonal FasL arrangements on DNA origami were designed exhibiting 5, 10, or 30 nm intermolecular FasL–FasL separation (see Figure 3; Figures S2, S4, and S5, Supporting Information for design and characterization). Samples were visualized by TEM (**Figure 3**A). Analyzing the images, we found ligand occupancies between 66 and 94% (Figure 3B), suggesting a robust formation of the anticipated nanoagent design. While for the 10 and 30 nm hexagonal designs the predominant ligand occupancy was six as expected (Figure 3B), for the 5 nm design, the predominant occupancy level was only four, most likely due to steric hindrance. We then probed the efficiency of apoptotic induction of the different FasL configurations. As can be seen in **Figure 4**A (upper left panel) 10 nm FasL spacing induces cell death significantly more efficiently (5× faster) than 5 or 30 nm spacing. These findings are in very good agreement with models of protein complex formation of the TNF superfamily, to which FasR and FasL belong.[15b,19] In a recent review by Vanamee et al., for example, the intermolecular distance between ligand-receptor pairs of the TNF superfamily was summed up to amount to ≈12 nm.[9] In the work of Gülcüler Balta et al. an optimal average FasL–FasL distance of about 9–11 nm for membrane anchored FasL was reported.[19] Yet, in the latter study FasL was free to diffuse laterally, whereas in the present work the spatial arrangement of DNA origami-bound FasL was fixed.

To decipher more precisely the effect of FasL number versus their arrangement, we fabricated two nanoagents displaying only two FasL with an inter-ligand distance of either 10 or 20 nm (derived from the 10 nm hexagon, see Figure S2, Supporting Information). Remarkably, reducing the number of FasL molecules per DNA origami by a factor of three appeared to have only a moderate effect on the average time-to-death (Figure 4A middle left panel) in comparison to different FasL hexagon spacings, suggesting that already a low number of FasL positioned at the correct inter-ligand distance can effectively induce apoptosis. A ranksum test yielded a highly significant deviation ($p < 0.001$) between the distributions of hexagonal FasL–DNA origami and FasL–DNA origami with only two ligands, whereas a less significant deviation ($p < 0.01$) was found for FasL–DNA origami displaying two FasL at inter-ligand distances of 10 and 20 nm, respectively. On average, DNA origamis displaying two FasL at 10 nm inter-ligand distance were more potent than those with 20 nm inter-ligand distance. Both of these structures were significantly more effective than origami-free, membrane-bound FasL (Figure 4A lower left panel). Based on these findings we conclude that the inter-ligand distances play a greater role than the number of FasL bound to DNA-origami.

To probe effects of FasL linker flexibility and coupling, we then repeated the above experiments using recombinant mv Streptavidin instead of wt Streptavidin (Figure 4B).[22] Here, mv Streptavidin possesses only one single functional binding

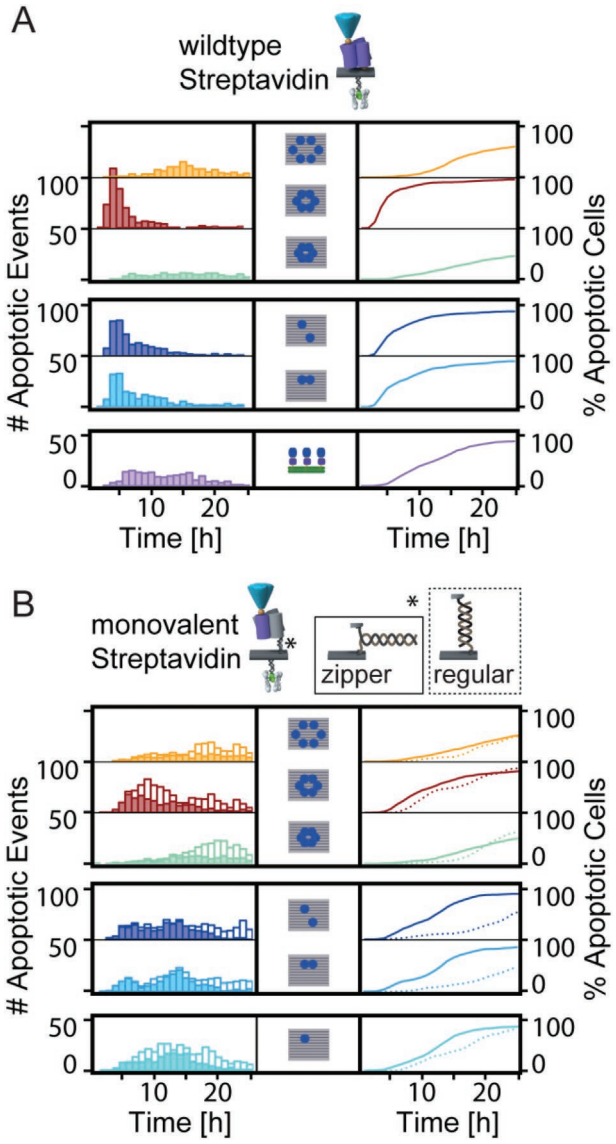

Figure 4. A) Histogram of time-to-death data, normalized to 200 cells per histogram, and percentage of apoptotic cells in population for different FasL–FasL distances arranged on DNA origami via wt Streptavidin: FasL hexagons with 10 nm intermolecular distance (red) exhibit highest efficiency in triggering cell apoptosis. FasL hexagons of 30 (orange) or 5 nm (mint) intermolecular distance, are least efficient. Two FasL arranged on the DNA origami with an inter-ligand distance of 20 (dark blue) or 10 nm distance (light blue) induce apoptosis faster compared to 10 nM membrane-bound FasL (purple). B) Same experiment as (A) but employing mv Streptavidin, either with a linker between origami and mv Streptavidin in zipper formation (solid histogram boxes and solid line) or with a regular hybridization linker distance of ≈7 nm (hollow histogram boxes and dotted line), indicated with an asterisk in the schematic. Additionally, data of a single FasL on DNA origami (cyan) is shown. The relative change between experiments in (B) follows the trend observed in (A) with broader distributions and shifted to longer times. ($n > 300$ cells/condition). Hollow histogram data was added to solid histogram data, all data was normalized to 200 cells/histogram.

pocket for Biotin, thus increasing positional control, and a thiol-maleimide coupling to a defined handle on the DNA origami with a 20 bp linker hybridizing either in a "zipper" or "regular" conformation (see schematic in Figure 4B; Figures S5 and S11, Supporting Information for characterization). The "regular" conformation enabled FasL spatial pre-orientation with 10 nm spatial flexibility (20 bp × 0.34 nm = 6.8 nm for DNA coupling in addition to the size of the Streptavidin), whereas the "zipper" configuration should result in reduced DNA linker flexibility (≈3 nm) compared to the "regular" hybridization (see Experimental Section). Histograms of the corresponding time-to-death data revealed that in both experiments with mv Streptavidin, apoptosis kinetics are significantly slower compared to that of the nanoagents formed with wt Streptavidin. However, the key observations for FasL–DNA origamis formed with wt Streptavidin are well reproduced: the 10 nm hexagon arrangement of FasL still appears as the most potent inducer of apoptosis, while for smaller and larger hexagonal arrangements apoptosis induction is suppressed. FasL–DNA origami displaying two ligands also resulted in slightly faster apoptosis rates than DNA origamis displaying only one FasL (Figure 4B lower right panel). Additionally, using the less flexible "zipper" configuration resulted in slightly faster apoptosis signal induction, compared to the more flexible "regular" configuration. Hence, mv Streptavidin coupling confirmed the general trend detected for the wt Streptavidin coupling, but the increasing linker flexibility and lack of precise ligand pre-orientation inhibits efficient apoptosis signal induction.

Intriguingly, several histograms of FasL nanoagents, especially those where two FasL or 6 FasL at 10 nm intermolecular distance are coupled to DNA origami, exhibited characteristic peaks indicating populations of cells with different apoptotic rates. To quantify the characteristic death times, all histograms were fitted with multiple Gaussians and the characteristic peak locations were extracted (Figure S8, Supporting Information). Two to three characteristic time points were detected per condition reflecting how fast the signal for apoptosis is initiated and transduced until the point of death occurs. The fastest time-to death for wt Streptavidin occurs after ≈3 h followed by a second peak between 5–8 h for the most efficient nanoagents. All other conditions exhibit less pronounced peaks at longer time scales. In case of mv Streptavidin the fastest time-to death occurs after 5–7 h for the most efficient nanoagents, whereas the other conditions again exhibit peaks at longer time scales. A possible mechanism for the appearance of characteristic peaks is that variable amounts of signaling molecules are activated resulting in different signaling cascades toward apoptosis (with or without mitochondrial involvement), as previously suggested.[23] Another explanation points to a diffusion-limited process, where bound FasL laterally rearranges on the SLM or in solution. Such process would require additional time until a signal initiation complex is formed. To further understand the origin of these peaks and to probe in how signal transduction depends on the receptor concentration, we studied the time-to-death kinetics of HeLa cells as a function of FasR expression (Figure S9, Supporting Information). We found that cells expressing FasR at different levels undergo apoptosis with no measurable correlation (Pearson coefficient $r = -0.04$ to -0.21) between FasR expression and time-to-death values.

Additionally, cell division did not have any visible effect on the time-to-death distribution: in Figure S10, Supporting Information, the time points of apoptosis for a whole cell population

is shown and cells of the same population dividing during the measurement time are indicated. Dividing cells undergo apoptosis at arbitrary time points and no correlation between the point of death and cell division was found. Interestingly, an occurrence of characteristic apoptotic timings was also observed by Márquez-Juarado et al. for TRAIL-induced apoptosis. Here, it was attributed to a variability of mitochondrial expression in the cell population.[24] Such variable mitochondrial expression levels may also occur in our cell line, even though we would expect its effects to appear in all histograms independent of the underlying FasL configuration. In total, our results confirm that apoptosis initiation sensitively depends on FasL arrangements, where intermolecular distance and molecular flexibility have a predominant effect compared to FasL number. Thus, pre-formed FasL clusters with the correct distance may facilitate the formation of a hexameric pattern of the DISC,[9,11d,14,15] whereas pre-arranged FasL patterns with spacings that do not match the predicted optimal FasL–FasL distance (e.g., 5 or 30 nm) suppress Fas-signaling possibly by spatial mismatch. Similar phenomena were also reported in the field of immunoactivation, where artificial arrays of antigens with defined spacing showed an enhanced immune response of B-cells.[8b]

Having identified the 10 nm hexagon (coupled via wt Streptavidin) as the most potent FasL configuration, we then proceeded to conduct further studies with this particular nanoagent. First, we probed how the cell signaling response could be optimized as a function of FasL–DNA origami concentration and performed a dose-response analysis for this 10 nm hexagon configuration. We exposed cells to decreasing amounts of FasL–DNA origami and calculated the surface concentration according to independent calibration experiments (Figure S12, Supporting Information). Intriguingly, we found a threshold-like behavior, where enhanced apoptosis rates as a function of surface concentration of DNA origamis are observed above 0.6 DNA origamis per μm^2 with no further increase between 0.6 and 4 DNA origamis per μm^2. Below 0.6 DNA origamis per μm^2 the apoptosis rate drops significantly from 0.21 $h^{-1} \pm 0.01\ h^{-1}$ to 0.05 $h^{-1} \pm 0.02\ h^{-1}$ (**Figure 5**A and Figure S13A, Supporting Information). These dose-response characteristics suggest that a surface concentration of $c_{Surface} = 0.6$ DNA origamis per μm^2 should be exceeded to maximize the apoptotic potency of nanoagents bound to the substrate. For a typical cell area of 1600 μm^2 this corresponds to about 100 DNA origamis per cell to efficiently induce apoptosis.[25]

Finally, and in view of nanoagent applications in cell biology and nanomedicine, it is important to probe the potency of nanoagents for signal induction in comparison to the naturally occurring free ligand in solution rather than bound to the SLM. Thus, we seeded cells on the SLM and incubated them with hexagonal FasL-nanoagents (10 nm inter-ligand spacing, no Cholesterol anchors) in the medium. Figure 5B and Figure S13B, Supporting Information show how the apoptosis rate increases continuously with increasing volume concentration and how it asymptotically reaches saturation. Fitting the data, we obtained an EC50 value of 0.09 nM ± 0.02 nM, which is clearly lower than an EC50 value of 10 nM reported for soluble FasL[26] and comparable to or even lower than values reported for other FasR targeting nanoagents.[20–21,27] Moreover, comparing FasL–DNA origamis incubated in solution with the cell response after

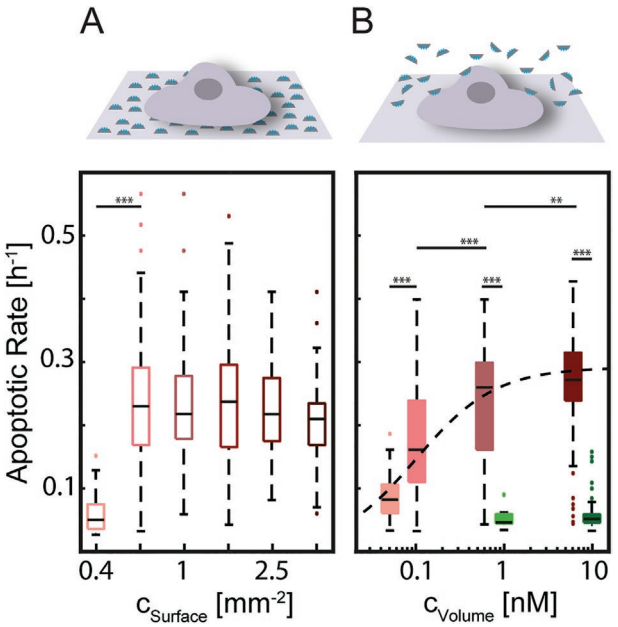

Figure 5. A) Boxplot with median of apoptotic rate for hexagonal FasL-nanoagent (10 nm spacing) at different surface concentrations of DNA origamis. The surface concentration was calculated from single molecule fluorescence analyses (Supporting Information). (n > 100 cells/condition). B) Apoptotic rate as a function of volume concentration of soluble FasL nanoagent (10 nm hexagon, red) compared to soluble FasL (green). Fit: $f(x) = m/(1+EC50/x)$ with $m = 0.29 \pm 0.02$ and half maximal effective concentration EC50 = 0.09 ± 0.02 nM, see text for further information (n > 100 cells/condition). Ranksum test: ***$p < 0.001$, **$p < 0.01$, *$p < 0.05$.

incubating origami-free, soluble FasL we find that FasL–DNA origami with hexagonal arrangement and 10 nm inter-ligand spacing exhibit a 6× higher apoptotic rate of 0.27 $h^{-1} \pm 0.04\ h^{-1}$ than soluble FasL (0.05 $h^{-1} \pm 0.01\ h^{-1}$) even when the latter was applied at a significantly higher volume concentration of 10 nM.

3. Conclusion

To conclude, we successfully engineered spatially pre-clustered FasL–DNA origami nanoagents as signaling platforms for cell death initiation. For the first time, systematic tuning of FasL nanometric spacing, their lateral organization, and linker flexibility enabled to identify benchmarks in cell signal initiation and sensitive changes in the corresponding cellular response. In particular, hexagonal FasL arrangements on DNA origami with 10 nm intermolecular spacing exhibited maximal potency as apoptosis inducer thereby confirming structural models of FasL signaling complex formation. Deviations from this intermolecular spacing lead to pronounced suppression of apoptosis signaling. Additionally, an increase in FasL linker flexibility, corresponding to a loss of FasL preorientation, turned out to be counterproductive for signal initiation. In future studies the direct conjugation of trimeric FasL to the DNA origami structure via the incorporation of unnatural amino acids or similar techniques could be explored to fully eliminate the effect of linkers. It is noteworthy that FasL–DNA origami required a

100× lower molar concentration to initiate apoptosis compared to the naturally occurring FasL molecules in solution and hence exhibited significantly higher potency. This constitutes a valuable result for future nanomedical approaches. We envision broad applicability of these nanoagents to decipher the physicochemical mechanisms underlying signal formation in cells, as for example the existence of local concentration thresholds or effects of molecular flexibility. Nanoagents may also provide unique insights into the structural organization of signaling complexes in cells as well as serve as efficient triggers of cluster-mediated cell responses in biological or medical applications.

4. Experimental Section

DNA Origami Fabrication: For the design of the DNA origami one-layer sheet (1LS) caDNAno 2.0 and the Picasso Software were used.[16b,28] The scaffold p7249 was purchased from tilibit nanosystems GmbH (Garching, Germany) and the staple oligonucleotides with the caDNAno generated sequences from Eurofins Genomic (Ebersberg, Germany). Also, biotinylated and fluorescently labeled oligonucleotides were produced by Eurofins Genomic. Cholesterol-TEG modified oligonucleotides were purchased from Biomers (Ulm, Germany). 10 nM scaffold was mixed with a 10× excess of staple oligonucleotides except fluorescent oligos (30× excess) and biotinylated oligonucleotides (80× excess) in a 1× TAE and 12.5 mM $MgCl_2$ buffer. The complementary handle sequences for the Cholesterol oligonucleotides were added with a final concentration of 8 nM. DNA origami structures were annealed in 16 h temperature ramp from 65 to 20 °C. Correct folding was screened either with gel electrophoresis or AFM. Unpurified structures were stored at 4 °C until further use. Origami were optionally purified 5× with Amicon Ultra-0.5 Centrifugal Filters (100 kDa, UFC510096, Merck Millipore). If origamis were purified, the folding concentration of the Cholesterol handles were added at 100 nM during folding.

AFM: First, DNA origami structures were purified with Amicon Ultra-0.5 Centrifugal Filters. Then, DNA origami structures were incubated on a mica at 1.5 nM concentration for 10 min. Both liquid and dry imaging were carried out on a Nanowizard Ultra Speed2 (Bruker Nano GmbH, Berlin, Germany). For liquid measurements 1.5 mL 1× TAE and 11 mM $MgCl_2$ (origami buffer) was added prior to imaging with tapping mode using either a FASTSCAN-B tip (Bruker Nano GmbH, Berlin, Germany) or a BL-AC40 TS tip (Oxford Instruments Asylum Research, Goleta CA, USA). For Figure 1C the sample was not purified after FasL addition resulting in adsorbed FasL surrounding the DNA origami sheets. For dry measurements samples were washed 3× with water, then blow-dried with nitrogen and a OMCL-AC160TS tip from Olympus Corporation (Shinjuko, Japan) was used.

Protein: Streptavidin was bought from Merck KGaA (Darmstadt, Germany) and the biotinylated FasL trimer was purchased from Apogenix (Heidelberg, Germany) and stored aliquoted and sterile at −20 °C. mv Streptavidin was produced as described by Sedlak et al. and stored in phosphate buffered silane (PBS) at 4 °C until further use.[22c] For thiol-maleimide coupling the mv Streptavidin was reduced with 1 mM TCEP over 30 min. Afterward it was desalted with Zeba spin desalting columns (ThermoFisherScientific, Waltham MA, USA) and transferred into coupling buffer (50 mM Na_2HPO_4, 50 mM NaCl, 10 mM EDTA, pH 7.2). 10× maleimide-DNA (Biomers, Germany) was added and incubated for 60 min. Access maleimide and coupling buffer were removed with Amicon Ultra-0.5 Centrifugal Filters and the functionalized mv Streptavidin stored in PBS at 4 °C until further use. In this form, the mv Streptavidin exhibiting a cysteine-side chain could then hybridize to complementary handle sequences protruding from the DNA origami.

Surface Functionalization: 18:1 (Δ9-cis) DOPC was purchased from Avanti Polar Lipids, Alabaster, USA dissolved in chloroform solution. 1-day prior measuring, 1 mg of the lipids was pipetted with a glass syringe from Hamilton (Reno, USA) to a chloroform cleaned glass vial. Afterward chloroform was evaporated by nitrogen gas and dried overnight under vacuum. Under sterile working conditions, precision cover glasses No. 1.5H (Paul Marienfeld GmbH & Co. KG, Lauda–Königshofen, Germany) were cleaned with UV grade Isopropanol and lens cleaning tissues, and were glued to ibidi stricky-Slide VI 0.4 (ibidi, Martinsried, Germany) and also stored overnight under vacuum. On the next day, 1 mL PBS was added to the dried lipids. The solution was vortexed, and tip sonicated on ice for at least 45 min until a clear solution was observable. In between, the slides were washed 5× with PBS. Then, 100 µL lipid solution was added to each channel and incubated for 1 h at room temperature. Afterward, channels were washed twice with sterile DI water to evoke an osmotic shock. Next the lipid bilayer was washed 5× with PBS before adding Cholesterol DNA (100 nM). After incubating for 15 min, channels were washed twice with PBS and twice with origami buffer. Next, unpurified DNA origami structures were incubated for 30 min to hybridize to the Cholesterol DNA on the membrane. Then, channels were washed twice with origami buffer, twice with buffer A (10 mM Tris-HCL, 100 mM NaCl, pH 8.0) to remove excess staples. Then Streptavidin was added at a concentration of 2.8 µM for wt Streptavidin and 60 nM for mv Streptavidin. After 10 min, the channels were rinsed with buffer A and FasL was incubated for 10 min at a concentration of 170 nM and subsequently washed with buffer A and with Leibovitz's-15 (L15) medium (ThermoFisherScientific, Waltham MA, USA) supplemented with 10% fetal bovine serum (FBS). This medium was commonly used during time-lapse microscopy and ensured if a physiological pH was maintained for the duration of the measurement.

Cell Culture and Time-Lapse Measurements: Hela cells were cultivated in DMEM Glutamax (ThermoFisherScientific, Waltham MA, USA) and 10% FBS. Cells were passaged twice a week and no longer cultivated than passage 30. For time-lapse measurements medium was changed to L15 medium supplemented with 10% FBS. Onto the functionalized surface 2000 cells were seeded per channel and anti-evaporation oil (ibidi, Martinsried, Germany) was added on top of the channel. Immediately, the slides were transferred to the microscope chamber preheated to 37 °C. Alternatingly, brightfield and fluorescence images were recorded every 10 min for 20–30 h.

Analysis: Cell death was measured by microscopy using transmitted light imaging and cell morphology analysis. Cell death kinetics were quantified from images taken every 10 min and by manually marking the first appearance of an apoptosis bubble indicating cell death. Marks were then automatically segmented and counted in ImageJ. The total number of cells was counted from 5–20 phase contrast images. Apoptotic cells were identified by recording the time point of irreversible cell blebbing and fragmentation of cell nuclei. Examination of the whole time series allowed to verify that the blebbing event was followed by cell death. Images were analyzed using the ImageJ timeseries analyzer plugin v3 as well as self-written routines in MATLAB (R2013b, The Math Works Inc, MA, USA). For cell-death kinetic curves, the percentage of apoptotic cells over time was plotted. For graphs showing the apoptotic rates [h^{-1}] first the time-to-death (τ_i) of each cell was determined and plotted in a histogram. Thereafter, the apoptosis rate ($k_i = 1/\tau_i$) was calculated for each cell.

Ab Binding Assay: Glass slides with SLM, DNA origami, mv/wt Streptavidin, and FasL were prepared as discussed above. Cy5 labeled FasL-Ab (CD178-APC human 130-096-458, Miltenyi Biotec) was diluted 1:100 in buffer A and incubated with the DNA origami nanoagents for 15 min. The slides were then washed with buffer A (300 µL) and immediately imaged at 100× magnification.

TEM Images: 100 µL 5 nM purified 1LS DNA origami were incubated for 30 min with 1.5 µM streptavidin (S4762-5MG, Sigma-Aldrich). Unbound Streptavidin was disposed of and the solution was concentrated using Amicon Ultra-0.5 Centrifugal Filters (100 kDa, UFC510096, Merck Millipore). For TEM imaging a solution was made containing 2 nM DNA origami- Streptavidin construct and 2% DMSO in TAE containing 12.5 mM $MgCl_2$.[29] The solution was incubated for 5 min on a freshly plasma activated grid. The grid was then stained for 60 s with 0.5% (m/v) uranyl formate for visualization by TEM (Jeol EM-1230, 40–120 KV fitted with a Gatan Orius CCD camera).

Supporting Information

Supporting Information is available from the Wiley Online Library or from the author.

Acknowledgements

The manuscript was written through contributions of all authors. R.L.M.B. was supported by a Deutsche Forschungsgemeinschaft (DFG) Fellowship through the Graduate School of Quantitative Biosciences Munich (QBM). T.L., J.O.R., and A.H.-J acknowledge the financial support of the Deutsche Forschungsgemeinschaft DFG through SFB1032 "Nanoagents" (A06 and A07). J.M.W. and A.H.-J acknowledge funding through the Emmy Noether program of the Deutsche Forschungsgemeinschaft DFG. C.M. acknowledges financial support of the Deutsche Forschungsgemeinschaft DFG through SFB1208 "Identity and Dynamics of Membrane Systems" (A12) and the "Freigeist fellowship" by Volkswagen Foundation. The authors thank S. Sedlak for providing mv Streptavidin for the measurements. The authors thank Joél Beaudouin (formerly at IBS, Grenoble) for providing stable cell lines and plasmids.

Open access funding enabled and organized by Projekt DEAL.

Conflict of Interest

The authors declare no conflict of interest.

Data Availability Statement

The data that supports the findings of this study are available in the supplementary material of this article.

Keywords

cell apoptosis, DNA origami, FasL/FasR, ligand-receptor interactions, signaling complex

Received: March 22, 2021
Revised: April 13, 2021
Published online: May 31, 2021

[1] a) M. L. Dustin, *Cancer Immunol. Res.* **2014**, *2*, 1023; b) C. Karathanasis, J. Medler, F. Fricke, S. Smith, S. Malkusch, D. Widera, S. Fulda, H. Wajant, S. J. L. van Wijk, I. Dikic, M. Heilemann, *Sci. Signaling* **2020**, *13*, eaax5647; c) R. Zhou, G. Yang, X. Guo, Q. Zhou, J. Lei, Y. Shi, *Science* **2019**, *363*, 857; d) I. Bethani, S. S. Skanland, I. Dikic, A. Acker-Palmer, *EMBO J.* **2010**, *29*, 2677.

[2] S. C. Balmert, S. R. Little, *Adv. Mater.* **2012**, *24*, 3757.

[3] a) D. Seo, K. M. Southard, J. W. Kim, H. J. Lee, J. Farlow, J. U. Lee, D. B. Litt, T. Haas, A. P. Alivisatos, J. Cheon, Z. J. Gartner, Y. W. Jun, *Cell* **2016**, *165*, 1507; b) D. Liße, C. Monzel, C. Vicario, J. Manzi, I. Maurin, M. Coppey, J. Piehler, M. Dahan, *Adv. Mater.* **2017**, *29*, 1700189; c) C. Monzel, C. Vicario, J. Piehler, M. Coppey, M. Dahan, *Chem. Sci.* **2017**, *8*, 7330.

[4] a) F. Pinaud, S. Clarke, A. Sittner, M. Dahan, *Nat. Methods* **2010**, *7*, 275; b) P. Le, S. J. Lim, B. C. Baculis, H. J. Chung, K. A. Kilian, A. M. Smith, *Nat. Commun.* **2019**, *10*, 909.

[5] M. A. McLean, M. C. Gregory, S. G. Sligar, *Annu. Rev. Biophys.* **2018**, *47*, 107.

[6] a) S. Nummelin, J. Kommeri, M. A. Kostiainen, V. Linko, *Adv. Mater.* **2018**, *30*, 1703721; b) K. F. Wagenbauer, F. A. S. Engelhardt, E. Stahl, V. K. Hechtl, P. Stommer, F. Seebacher, L. Meregalli, P. Ketterer, T. Gerling, H. Dietz, *ChemBioChem* **2017**, *18*, 1873; c) N. C. Seeman, *Nature* **2003**, *421*, 427.

[7] a) A. R. Chandrasekaran, *Nanoscale* **2016**, *8*, 4436; b) J. B. Trads, T. Tørring, K. V. Gothelf, *Acc. Chem. Res.* **2017**, *50*, 1367; c) S. Modi, D. Bhatia, F. C. Simmel, Y. Krishnan, *J. Phys. Chem. Lett.* **2010**, *1*, 1994; d) E. Ambrosetti, G. Bernardinelli, I. Hoffecker, L. Hartmanis, R. Sandberg, B. Högberg, A. I. Teixeira, *Nat Nanotechnol.* **2021**, *16*, 85; e) V. Linko, M. Eerikäinen, M. A. Kostiainen, *Chem. Commun.* **2015**, *51*, 5351; f) B. Saccà, R. Meyer, M. Erkelenz, K. Kiko, A. Arndt, H. Schroeder, K. S. Rabe, C. M. Niemeyer, *Angew. Chem.* **2010**, *49*, 9378; g) B. Saccà, C. M. Niemeyer, *Chem. Soc. Rev.* **2011**, *40*, 5910; h) A. Shaw, I. T. Hoffecker, I. Smyrlaki, J. Rosa, A. Grevys, D. Bratlie, I. Sandlie, T. E. Michaelsen, J. T. Andersen, B. Högberg, *Nat. Nanotechnol.* **2019**, *14*, 184.

[8] a) A. Shaw, V. Lundin, E. Petrova, F. Fordos, E. Benson, A. Al-Amin, A. Herland, A. Blokzijl, B. Hogberg, A. I. Teixeira, *Nat. Methods* **2014**, *11*, 841; b) R. Veneziano, T. J. Moyer, M. B. Stone, E.-C. Wamhoff, B. J. Read, S. Mukherjee, T. R. Shepherd, J. Das, W. R. Schief, D. J. Irvine, M. Bathe, *Nat. Nanotechnol.* **2020**, *15*, 716; c) A. Angelin, S. Weigel, R. Garrecht, R. Meyer, J. Bauer, R. K. Kumar, M. Hirtz, C. M. Niemeyer, *Angew. Chem., Int. Ed.* **2015**, *54*, 15813; d) P. Lanzerstorfer, U. Müller, K. Gordiyenko, J. Weghuber, C. M. Niemeyer, *Biomolecules* **2020**, *10*, 540.

[9] E. S. Vanamee, D. L. Faustman, *Sci. Signaling* **2018**, *11*, eaao4910.

[10] a) B. B. Aggarwal, *Nat. Rev. Immunol.* **2003**, *3*, 745; b) J.-L. Bodmer, P. Schneider, J. Tschopp, *Trends Biochem. Sci.* **2002**, *27*, 19; c) M. E. Peter, P. H. Krammer, *Cell Death Differ.* **2003**, *10*, 26; d) M. E. Guicciardi, G. J. Gores, *FASEB J.* **2009**, *23*, 1625.

[11] a) E. Brint, G. O'Callaghan, A. Houston, *Cell. Mol. Life Sci.* **2013**, *70*, 4085; b) D. B. Chappell, N. P. Restifo, *Cancer Immunol. Immunother.* **1998**, *47*, 65; c) S. Meynier, F. Rieux-Laucat, *Immunol. Rev.* **2019**, *287*, 50; d) M. E. Peter, A. Hadji, A. E. Murmann, S. Brockway, W. Putzbach, A. Pattanayak, P. Ceppi, *Cell Death Differ.* **2015**, *22*, 549.

[12] a) M. M. F. Qadir, S. Álvarez-Cubela, D. Klein, G. Lanzoni, C. García-Santana, A. Montalvo, F. Pláceres-Uray, E. M. C. Mazza, C. Ricordi, L. A. Inverardi, R. L. Pastori, J. Domínguez-Bendala, *Cell Rep.* **2018**, *22*, 2408; b) A. Martin-Villalba, E. Llorens-Bobadilla, D. Wollny, *Trends Mol. Med.* **2013**, *19*, 329.

[13] J. P. Guegan, C. Ginestier, E. Charafe-Jauffret, T. Ducret, J. F. Quignard, P. Vacher, P. Legembre, *Semin. Cancer Biol.* **2020**, *60*, 121.

[14] a) L. Wang, J. K. Yang, V. Kabaleeswaran, A. J. Rice, A. C. Cruz, A. Y. Park, Q. Yin, E. Damko, S. B. Jang, S. Raunser, C. V. Robinson, R. M. Siegel, T. Walz, H. Wu, *Nat. Struct. Mol. Biol.* **2010**, *17*, 1324; b) Q. Fu, T. M. Fu, A. C. Cruz, P. Sengupta, S. K. Thomas, S. Wang, R. M. Siegel, H. Wu, J. J. Chou, *Mol. Cell* **2016**, *61*, 602.

[15] a) A. Algeciras-Schimnich, L. Shen, B. C. Barnhart, A. E. Murmann, J. K. Burkhardt, M. E. Peter, *Mol. Cell. Biol.* **2002**, *22*, 207; b) F. L. Scott, B. Stec, C. Pop, M. K. Dobaczewska, J. J. Lee, E. Monosov, H. Robinson, G. S. Salvesen, R. Schwarzenbacher, S. J. Riedl, *Nature* **2009**, *457*, 1019.

[16] a) P. W. K. Rothemund, *Nature* **2006**, *440*, 297; b) S. M. Douglas, A. H. Marblestone, S. Teerapittayanon, A. Vazquez, G. M. Church, W. M. Shih, *Nucleic Acids Res.* **2009**, *37*, 5001.

[17] N. V. Voigt, T. Torring, A. Rotaru, M. F. Jacobsen, J. B. Ravnsbaek, R. Subramani, W. Mamdouh, J. Kjems, A. Mokhir, F. Besenbacher, K. V. Gothelf, *Nat. Nanotechnol.* **2010**, *5*, 200.

[18] a) S. Kocabey, S. Kempter, J. List, Y. Xing, W. Bae, D. Schiffels, W. M. Shih, F. C. Simmel, T. Liedl, *ACS Nano* **2015**, *9*, 3530; b) S. Kempter, A. Khmelinskaia, M. T. Strauss, P. Schwille, R. Jungmann, T. Liedl, W. Bae, *ACS Nano* **2019**, *13*, 996; c) A. Johnson-Buck, S. Jiang, H. Yan, N. G. Walter, *ACS Nano* **2014**, *8*, 5641.

[19] G. S. Gulculer Balta, C. Monzel, S. Kleber, J. Beaudouin, E. Balta, T. Kaindl, S. Chen, L. Gao, M. Thiemann, C. R. Wirtz, Y. Samstag, M. Tanaka, A. Martin-Villalba, *Cell Rep.* **2019**, *29*, 2295.
[20] N. Holler, A. Tardivel, M. Kovacsovics-Bankowski, S. Hertig, O. Gaide, F. Martinon, A. Tinel, D. Deperthes, S. Calderara, T. Schulthess, J. Engel, P. Schneider, J. Tschopp, *Mol. Cell. Biol.* **2003**, *23*, 1428.
[21] N. Zhang, Y. Yang, Z. Wang, J. Yang, X. Chu, J. Liu, Y. Zhao, *J. Controlled Release* **2019**, *309*, 48.
[22] a) M. Howarth, D. J. Chinnapen, K. Gerrow, P. C. Dorrestein, M. R. Grandy, N. L. Kelleher, A. El-Husseini, A. Y. Ting, *Nat. Methods* **2006**, *3*, 267; b) S. M. Sedlak, M. S. Bauer, C. Kluger, L. C. Schendel, L. F. Milles, D. A. Pippig, H. E. Gaub, *PLoS One* **2017**, *12*, e0188722; c) S. M. Sedlak, L. C. Schendel, M. C. R. Melo, D. A. Pippig, Z. Luthey-Schulten, H. E. Gaub, R. C. Bernardi, *Nano Lett.* **2019**, *19*, 3415.
[23] a) C. Scaffidi, S. Fulda, A. Srinivasan, C. Friesen, F. Li, K. J. Tomaselli, K. M. Debatin, P. H. Krammer, M. E. Peter, *EMBO J.* **1998**, *17*, 1675; b) P. J. Jost, S. Grabow, D. Gray, M. D. McKenzie, U. Nachbur, D. C. Huang, P. Bouillet, H. E. Thomas, C. Borner, J. Silke, A. Strasser, T. Kaufmann, *Nature* **2009**, *460*, 1035.
[24] S. Márquez-Jurado, J. Díaz-Colunga, R. P. das Neves, A. Martinez-Lorente, F. Almazán, R. Guantes, F. J. Iborra, *Nat. Commun.* **2018**, *9*, 389.
[25] T. T. Puck, P. I. Marcus, S. J. Cieciura, *J. Exp. Med.* **1956**, *103*, 273.
[26] W. Liu, U. Ramagopal, H. Cheng, J. B. Bonanno, R. Toro, R. Bhosle, C. Zhan, S. C. Almo, *Structure* **2016**, *24*, 2016.
[27] M. Chodorge, S. Züger, C. Stirnimann, C. Briand, L. Jermutus, M. G. Grütter, R. R. Minter, *Cell Death Differ.* **2012**, *19*, 1187.
[28] J. Schnitzbauer, M. T. Strauss, T. Schlichthaerle, F. Schueder, R. Jungmann, *Nat. Protoc.* **2017**, *12*, 1198.
[29] L. Mallik, S. Dhakal, J. Nichols, J. Mahoney, A. M. Dosey, S. Jiang, R. K. Sunahara, G. Skiniotis, N. G. Walter, *ACS Nano* **2015**, *9*, 7133.